The functional micro-organization of grid cells revealed by cellular-resolution imaging

James G. Heys[1], **Krsna V. Rangarajan**[1,2], and **Daniel A. Dombeck**[1,*]

[1]Department of Neurobiology, Northwestern University, Evanston, IL

Summary

Establishing how grid cells are anatomically arranged, on a microscopic scale, in relation to their firing patterns in the environment would facilitate a greater micro-circuit level understanding of the brain's representation of space. However, all previous grid cell recordings used electrode techniques that provide limited descriptions of fine-scale organization. We therefore developed a technique for cellular-resolution functional imaging of medial entorhinal cortex (MEC) neurons in mice navigating a virtual linear track, enabling a new experimental approach to study MEC. Using these methods, we show that grid cells are physically clustered in MEC compared to non-grid cells. Additionally, we demonstrate that grid cells are functionally micro-organized: The similarity between the environment firing locations of grid cell pairs varies as a function of the distance between them according to a "Mexican Hat" shaped profile. This suggests that, on average, nearby grid cells have more similar spatial firing phases than those further apart.

Introduction

In vivo imaging experiments are beginning to reveal how the encoding properties and flexibility of circuits are related to the anatomical functional organization of their neurons on the micro-circuit scale (positioning of neurons on the 10's of microns scale). For example, in high-level association brain regions which form complex and flexible representations from multi-modal input, only a random or limited functional micro-arrangement has been observed (i.e. the physical positioning of neurons with respect to each other is not strongly related to their encoding properties (Dombeck et al., 2010; Harvey et al., 2012)). In contrast, in lower-level sensorimotor regions which form relatively simple and stable representations from lower modality input, a relatively high degree of functional micro-arrangement has been observed (i.e. neurons with similar encoding properties are spatially clustered) (Bonin et al., 2011; Dombeck et al., 2009; Hira et al., 2013; Issa et al., 2014; Komiyama et al., 2010; Sato et al., 2007). The medial entorhinal cortex (MEC), however, is a high-level association brain region that integrates multi-modal input, but it forms relatively simple and stable representations, making it unclear if the functional micro-organization of its neurons will resemble high-level association or lower-level sensorimotor regions.

Grid cells in the MEC generate a metric for representing an animal's local spatial environment. These cells fire selectively when an animal visits locations arranged on the vertices of a repeating regular triangular lattice, tiling the floor of the environment (Fyhn et al., 2004; Hafting et al., 2005). Determining the anatomical location and circuit organization of grid cells in the MEC in relation to their environment firing patterns has been the focus of numerous experiments and computational models (Burak and Fiete, 2009; Burgalossi et al., 2011; Couey et al., 2013; Fuhs and Touretzky, 2006; Garden et al., 2008; Giocomo et al., 2007; Guanella et al., 2007; Hafting et al., 2005; Kitamura et al., 2014; Pastoll et al., 2013; Ray et al., 2014; Stensola et al., 2012; Yoon et al., 2013). For example, the initial discovery of grid cells demonstrated that their spatial periodicity changes systematically across the dorsal-ventral axis of the MEC and more recent studies have demonstrated that these changes occur in discrete steps, suggesting that the MEC contains numerous independent grid cell modules, each with different grid firing properties and each occupying ~300–500 micron regions in the MEC (Hafting et al., 2005; Stensola et al., 2012). Consistent with the idea of functional modules, grid cells recorded on the same or nearby tetrode (hundreds of microns apart) display coordinated changes in grid field properties in response to changes to the animal's local environment (Yoon et al., 2013). Together, these findings lent support to previously existing computational models in which each grid cell functional module consists of a low-dimensional continuous attractor network (CAN). Thus knowledge of the functional organization of grid cells on the macroscopic scale (100's of microns to millimeters) has provided support for CAN models of grid cells.

Due largely to technical limitations associated with studying smaller spatial scales in the MEC, it remains unclear if or how grid cells are functionally organized on the micro-circuit scale. For example, while no clear topography of grid phase has been observed on the macroscopic scale (Hafting et al., 2005), it is unknown whether any grid phase topography exists on finer scales (Moser et al., 2014). Further, while anatomical studies have suggested that grid cells may physically cluster together in the MEC (Kitamura et al., 2014; Ray et al., 2014), more direct evidence for grid cell clustering is lacking. Thus, methods capable of functional measurements at finer scales in the MEC should provide important new information about the grid cell network and enable a greater micro-circuit level description of grid cell firing.

Results

Chronic cellular resolution imaging of MEC in behaving mice

To allow for measurements of the functional micro-organization of grid cells we developed a chronic imaging window that allows for cellular-resolution two-photon imaging of neuronal activity in MEC of behaving mice. Imaging MEC directly through the dorsal cortical surface is complicated by the large transverse sinus and the physical depth of MEC (~1.5 mm below the dorsal surface). Removing overlaying cortical tissue to reach MEC is not desirable because this tissue forms direct connections to MEC and, since no physical barrier exists between MEC and the overlaying cortical tissue, acute damage to MEC would likely result. Instead, we developed a method to image from the caudal side of the brain in which no cortical tissue was disturbed and the dura surrounding the cortex was left intact.

We performed a craniotomy, removed a portion of the cerebellum and chronically implanted a microprism (Chia and Levene, 2009) onto the caudal surface of MEC (Figure 1A). Using an overhead two-photon microscope (Figure 1B), the microprism provided optical access to the MEC with the imaging plane parallel to the caudal surface. Neurons were labeled with a genetically encoded calcium indicator (GCaMP-6f) delivered via an adeno-associated virus targeted to MEC. Fields of labeled neurons could often be imaged through the MEC microprism (Figure 1D) for many weeks and at depths of up to ~300–400 μm (from the caudal dura surface).

After virus infection and MEC microprism implantation, the mice were trained to run along a 4 m or 5 m virtual linear track for water rewards. The mice were head-restrained, but were able to run on a cylindrical treadmill. Their movement on the treadmill caused movement along the track, which was displayed on surrounding screens (Domnisoru et al., 2013; Harvey et al., 2009) (Figure 1B,C). At the end of the track, the mice received a small water reward, and were then "teleported" back to the beginning of the track for the start of another traversal.

Once mice routinely ran along the track (5.1 ± 1.5 days of training (mean $\pm$ SEM), range: 2–14 days), imaging sessions commenced. The two-photon imaging plane (fields of view: 380–450 μm medial-lateral by 300–370 μm dorsal-ventral; 16 fields in 7 mice) was positioned in MEC layer 2 (104 ± 20 μm deep from the caudal dura surface, mean $\pm$ STD) where the activity of populations of neurons were recorded using time-series movies (14.4 or 28.8 frames/sec) acquired during track traversals (1.6 ± 0.5 track traversals/min, 24.0 ± 6.9 cm/sec during imaging sessions; 20.4 ± 7.2 track traversals per 12.4 ± 1.2 min time-series recording) (Figure 1D,E,F). Registration of two-photon imaging fields with respect to the caudal surface vasculature along with post-mortem staining and slicing was used to verify that the imaging fields were located in MEC (Figure 1D,E, Figure S1A and Supplemental Methods).

Somatic calcium transients were frequently observed in many individual neurons across the population during track traversals (70.1 ± 22.0 active neurons/field, mean $\pm$ STD; range of 42 to 106 active neurons/field) (Figure 1D,F). Somatic calcium transients from cortical neurons labeled with GCaMP-6f have previously been shown to report action potential firing (Chen et al., 2013), though in a different neuron type than studied here in MEC. The calcium transients we recorded from MEC neurons are consistent with an action potential source (Figure 1F). They varied in amplitude (Figure S1C, mean $\pm$ STD = $83.32 \pm 62.82\%$ F/F), consistent with a difference in the number of underlying action potentials, and varied in duration (Figure S1D, mean $\pm$ STD = 5.0 ± 4.7 sec), consistent with the summation of multiple transients. Further, averaging our smallest-amplitude somatic calcium transients produced a trace (Figure. S1E) similar to what is expected from a single somatic action potential based on previous combined cell-attached and imaging measurements (Chen et al., 2013) (however, single or double action potentials may not always be detected under our imaging conditions). We therefore used somatic calcium transients as a measure of action potential firing in populations of MEC layer 2 neurons during linear track traversals.

Identification and characterization of optically recorded grid cells

During track traversals, many neurons fired at several specific locations along the track. The firing in these neurons repeated at the same location across many traversals and formed multiple distinct firing fields along the track that were highly similar to previously reported mean linear track firing patterns from identified grid cells in MEC (Brun et al., 2008; Domnisoru et al., 2013; Hafting et al., 2008) (Figure 2A–C, Figure S2 and S3). In order to classify these neurons as grid cells based on their mean firing patterns along the virtual linear track, we made use of a previously reported classifier which was developed for the same purpose (Domnisoru et al., 2013). The classifier was created based on single unit recordings from grid cells in mice navigating a real two-dimensional open field environment and recordings from the same cells along a virtual linear track, similar to ours. Making use of this classifier (see Methods), we identified 259 neurons as grid cells (out of 1122 identified active neurons) across 16 imaging fields (16 ± 7 grid cells/field (mean ± STD), range of 9 to 34 grid cells/field) in 7 mice. The classifier (Domnisoru et al., 2013) was designed based on measurements using different recording methods (extracellular tetrode recordings) and possibly from more dorsal regions of the MEC compared to the recordings presented here, and therefore the grid classified cells should technically be referred to as "putative grid cells"; however because of the many similarities between the cells recorded here and those of previous studies (see below), we refer to these cells simply as "grid cells".

Consistent with both intra- and extra-cellular recordings of grid cells in virtual and real environments (Figure S2F,G), our optically recorded grid cell firing fields along the linear track were characterized by a mean width of 44 ± 24 cm (mean ± STD, n = 552), a mean number of fields per meter of 0.5 ± 0.1 (mean ± STD, n=259) (Figure 2D,E) and a significant negative relationship between the width and number of fields (Figure 2F; n = 259; $P < 0.01$, $\rho = -0.34$, Spearman Rank Correlation Coefficent; linear fit: significant negative linear slope within 95% confidence bounds). Our optically recorded grid cells also exhibited other properties consistent with previously published observations (Brun et al., 2008; Domnisoru et al., 2013; Fyhn et al., 2008; Hafting et al., 2008) (greater number of grid fields in long versus short tracks, similar field widths in long and short tracks, and little change in spatial firing properties along the dorsal-ventral axis over the short distances studied here) (Figure S2A–D). Among individual traversals in which a given cell exhibited at least one significant transient, our optically recorded grid cells fired in only a single grid field on 58% of the traversals and in multiple grid fields on 42% of the traversals. A similar quantification of single trial data is not readily available from past studies for comparison, however, a qualitative comparison to previous studies using rodents running along real or virtual linear tracks demonstrates that many grid cells often fire in only single fields or have little or no AP firing in a given grid field on many traversals (Domnisoru et al., 2013; Hafting et al., 2008). Finally, recent modeling work appears to show that the mean firing pattern of a particular grid cell on a 1D linear track is likely the result of a linear traversal (slice) through the cell's grid field pattern in a 2D environment (Domnisoru et al., 2013; Lewallen et al., 2013; Yoon et al., 2013), suggesting that the firing mechanisms underlying the track activity pattern in 1D is the same as the mechanisms that leads to the grid field firing in an open field environment. Thus our imaging methods are capable of recording from populations of grid cells in MEC that have firing characteristics similar to those

recorded in freely moving rodents and their track firing patterns likely result from the same mechanisms driving firing in open field environments.

Grid cells are physically clustered in MEC

With the ability to identify the anatomical location of grid cells and non-grid cells (i.e. track active neurons, many with spatial firing fields, which were not classified as grid cells) in the MEC on the micro-circuit scale, we next assessed the spatial micro-organization of neurons within and between these two groups. We focused on 8 imaging fields with similar field of view sizes (375 ± 7 μm by 298 ± 5 μm sizes) to minimize cell-cell distance variance. When the neurons in the different imaging fields were false colored according to their grid or non-grid identity (3 example fields shown in Figure 3A), grid cells appeared to cluster together more than non-grid cells. To quantify the degree of clustering within each of the fields, we calculated the mean of the spatial separation between all grid cell pairs in each field and compared it to the mean separation between all non-grid cell pairs. For each of the three example fields shown in Figure 3A, the mean grid cell – grid cell distance was significantly less than the mean non-grid cell – non-grid cell distance (130 ± 3 μm vs 158 ± 2 μm, 115 ± 7 μm vs 146 ± 2 μm, 110 ± 4 μm vs 130 ± 2 μm (mean $\pm$ SEM) for grid – grid vs. non-grid – non-grid distances for examples in Figure 3A, top to bottom, respectively; $P < 0.01$ for all three examples, Student's t-test). Due to the relatively large spatial extent of each of the cell groups (grid cells and non-grid cells), these small but significant differences between the intra- and inter group neuron – neuron distances are exactly what is expected, even for highly spatially separated groups (Dombeck et al., 2009). A similar effect in which grid cell – grid cell distance was less than non-grid cell – non-grid cell distance was observed in 6 out of the 8 imaging fields (Figure 3C). When results from all 8 of the imaging fields were combined, an average effect similar to that seen in the above individual examples (Figure 3A) was observed: grid cell – grid cell distance was significantly less than non-grid cell – non-grid cell distance (Figure 3B; 134 ± 2 μm vs 152 ± 1 μm (mean $\pm$ SEM), $P < 0.01$, Student's t-test). A similar result was observed when only distances in the dorsal-ventral or medial-lateral directions were examined (dorsal-ventral grid cell – grid cell distance: 89 ± 2 μm vs dorsal-ventral non-grid cell – non-grid cell distance: 99 ± 1 μm, mean $\pm$ SEM, $P < 0.01$, Student's t-test; medial-lateral grid cell – grid cell distance: 81 ± 2 μm vs medial-lateral non-grid cell – non-grid cell distance: 95 ± 1 μm, mean $\pm$ SEM, $P < 0.01$, Student's t-test). Additionally, when mean neuron – neuron distances were measured from randomly selected groups of neurons in each imaging field (the number of randomly selected neurons in each field equal to the number of grid cells in the field), the mean intra-random neuron group distances were nearly always greater than the mean grid cell – grid cell distances (996 out of 1000 random samples; $P < 0.01$ from bootstrapping; mean grid cell-grid cell distance: 134 ± 2 μm; mean random neuron-neuron distance: 147.0 ± 0.2 μm, mean $\pm$ SEM). Thus, grid cells are more physically clustered in the MEC than non-grid cells, and grid cells are more physically clustered in the MEC than would be expected by randomly selecting subpopulations.

Grid cells are functionally micro-organized in MEC

With the ability to measure the firing patterns of grid cells in the animal's local environment and determine their anatomical location in the MEC on the micro-circuit scale, we next

assessed the functional micro-arrangement of grid cells. For all classified grid cells in each imaging field, we calculated all pairwise mean track firing pattern (mean F/F versus track position) correlations (see Figure 4A for example pairs) and pairwise distances between the cells in the MEC and then we combined the results from all 16 imaging fields. When we plotted mean firing pattern correlation as a function of mean distance between the grid cells, we found a relationship characterized by a "Mexican Hat" profile (Figure 4B): nearby grid cells (<~50 μm) fire at more similar locations in the environment and thus on average have a relatively high correlation between their mean track firing patterns, grid cells separated by an intermediate distance (~100–150 μm) fire at more dissimilar locations and thus on average have a lower correlation and grid cells separated by a larger distance (~200–250 μm) display a wide-range of firing location overlap and thus on average have an intermediate correlation. A qualitatively similar Mexican Hat profile was also observed in both the medial-lateral and dorsal-ventral directions (Figure S4C and S4D), though interestingly the trough of the profile was found at a greater distance in the medial-lateral compared to dorsal-ventral direction.

In order to determine the statistical significance of this relationship, within each imaging field the grid cells were left in the same anatomical location but were randomly assigned the mean track firing pattern of a different grid cell. When this randomization procedure was repeated 1000 times, the experimental data firing pattern correlation versus distance profile (Figure 4B, black) was found to be statistically significantly different than the randomized data profile (Figure 4B, red) ($P < 10^{-12}$, Kolmogorov–Smirnov test). The track firing pattern correlations between the experimental and randomized data were also compared within windows (30 μm in width) around each single micron step for significance (** in Figure 4B, $P < 0.01$, from bootstrapping) and position bins were chosen containing all micron steps in contiguous regions of the experimental data where the correlations were significantly above, below or not different than the randomized data: track firing pattern correlations for grid cells separated by 20–50 μm, 111–147 μm, or 200–256 μm were significantly larger, smaller or not different than the correlations in the randomized data, respectively (Figure 4B). Further, the correlations between mean track firing patterns for nearby grid cells (20–50 μm) was significantly greater than correlations for grid cells separated by intermediate distances (111–147 μm) (Figure 4C), while the correlations for nearby and intermediate distance separated cells were significantly higher and lower than correlations for cells separated by larger distances (200–256 μm) (Figure 4C, $P < 10^{-9}$, One-way ANOVA; $P < 0.01$, Post-hoc Tukey-Kramer), respectively. Importantly, the same Mexican Hat correlation profile was not observed between non-grid cells (Figure S4A and S4B). Thus, the Mexican Hat shaped relationship between pairwise grid cell – grid cell distance and mean track firing pattern correlation is present in both the medial-lateral and dorsal-ventral directions, is statistically significant and is not seen in non-grid cells from the same imaging fields.

Discussion

Grid cells display physical clustering and functional micro-organization

By developing novel optical methods for functional imaging with cellular resolution in the MEC of behaving mice, we were able to record the firing patterns of large populations of

MEC neurons during navigation along a virtual linear track. We classified many of the neurons as grid cells based on their firing patterns along the virtual linear track and demonstrated that grid cells in the MEC are functionally micro-organized. Therefore, the functional micro-organization of this class of neurons in the MEC is more reminiscent of functional micro-clustering previously observed in sensorimotor regions (Bonin et al., 2011; Dombeck et al., 2009; Hira et al., 2013; Issa et al., 2014; Komiyama et al., 2010; Sato et al., 2007) rather than the random or limited functional micro-arrangement observed in high-level association brain regions (Dombeck et al., 2010; Harvey et al., 2012). Interestingly, similar investigations of place cells in the hippocampus found little or no relationship between cell-cell distance and environment firing overlap (Dombeck et al., 2010; Redish et al., 2001). While such seemingly random positioning of cell bodies in the hippocampus may reflect the high-degree of plasticity required for forming associations to encode new experiences, the more functionally organized structure of the MEC could be useful for maintaining the relatively constant regular representation seen in grid cells across dynamic environments. Thus differences in encoding demands may be reflected in the anatomical micro-arrangement of neurons of a given micro-circuit, possibly due to the variable influence of fundamental constraints such as wiring distance minimization, network flexibility and information storage capacity.

Our imaging methods also revealed that grid cells are physically clustered in layer 2 of the MEC compared to non-grid cells. Previous studies (Kitamura et al., 2014; Ray et al., 2014) have demonstrated physical clustering of calbindin positive MEC layer 2 neurons, which are likely pyramidal neurons (Varga et al., 2010), but no clustering of reelin positive neurons, which are likely stellate cells (Varga et al., 2010). Separate intracellular grid cell patch clamp studies (Domnisoru et al., 2013; Schmidt-Hieber and Häusser, 2013) demonstrated that the grid cell population is composed of both stellate cells and pyramidal neurons. Thus together, these studies suggest that the grid cell population is composed of two subpopulations of neurons, one that forms spatially clustered groups and the other that is more uniformly distributed. Therefore, when examined across the population, the combined results of these previous studies predict some degree of spatial clustering of grid cells, a prediction which is supported by the results presented here.

Grid cell functional micro-organization suggests nearby grid cells have similar spatial phase

Spatial phase is a measure of a grid cell's mean firing pattern in a *two-dimensional* environment and refers to the location of the grid vertices with respect to another grid cell (of the same spacing and orientation). What then can our results using the mean track firing pattern along a *one-dimensional* track tell us about the relative differences in spatial phase of neighboring grid cells? Recent analysis (Domnisoru et al., 2013) and modeling (Lewallen et al., 2013; Yoon et al., 2013) demonstrate that the mean firing pattern of a particular grid cell on a 1D linear track is likely the result of a linear traversal (slice) through the cell's grid field pattern in a 2D environment. Based on this result and additional data demonstrating that grid spacing and orientation of nearby grid cells is highly similar (Hafting et al., 2005; Stensola et al., 2012; Yoon et al., 2013), the correlation between the mean firing patterns of two grid cells along a linear track is likely related to the similarity between their grid phases

in a two-dimensional environment (Figure S5): high or low linear track firing pattern correlations arise from in- or out-of-phase grid cells, respectively (i.e. linear track correlation is a monotonically increasing function of 2D phase similarity). Therefore, our results demonstrating that the linear track firing patterns of nearby grid cells in MEC are on average more highly correlated than cells separated by greater distances suggests that grid phase is not randomly distributed across the grid cell population, but instead nearby grid cells, on average, have more similar spatial firing phases than those further apart.

Comparison to other methods

Previous grid cell studies have used electrode methods, either juxtacellular recordings capable of functional measurements followed by morphological study (Burgalossi et al., 2011), intracellular recordings capable of sub-threshold membrane potential dynamics measurements (followed by morphological study) (Domnisoru et al., 2013; Schmidt-Hieber and Häusser, 2013), or tetrode recordings capable of simultaneous recordings from populations of grid cells (Hafting et al., 2005; Stensola et al., 2012). Interestingly, a previous study using tetrodes found that the grid phases of grid cells simultaneously recorded from the same tetrode were apparently not related (Hafting et al. 2005). This is in contrast to our results which suggest that, on average, nearby grid cells have similar spatial phase. It is likely that this discrepancy arises from the differences between the recording methods. Two-photon imaging is capable of sub-cellular resolution and simultaneous recording from hundreds of neurons within a small region (100's of microns). These recording capabilities are well suited to studying fine scale functional organization (Figure 3, 4). By contrast, tetrodes appear to sparsely sample from only a few of the neurons within a ~50–100 micron radius of the recording sites (Henze et al., 2000; Mechler et al., 2011). The small number of recorded neurons and relatively low spatial resolution (> ~100 microns) likely make observing fine scale functional organization, such as that seen in Figure 4, difficult or impossible with tetrodes.

Combining our micro-prism MEC imaging approach with miniaturized microscopes (Sawinski et al., 2009; Ziv et al., 2013) may allow for recordings of grid cells in freely moving animals. Such recordings could enable grid cell population imaging experiments during open field navigation, providing direct measures of grid phase, spacing and orientation. 2D open field experiments have not yet been demonstrated for head-restrained animals navigating in virtual reality. Though future technical advances may allow for 2D spatial behaviors and the formation of 2D neural spatial representations, it is possible that the lack of vestibular input in head-restrained animals, which can be used to update heading direction, may make such studies difficult and may limit studies to 1D environments. On the other hand, experiments using virtual reality and table top microscopes can take advantage of the ability to manipulate environmental stimuli in ways not possible in real environments (Dombeck and Reiser, 2012) and rapidly adopt new optical techniques (Göbel and Helmchen, 2007; Ji et al., 2012; Katona et al., 2012). Thus, we anticipate that our imaging methods will open a new avenue for probing MEC networks by allowing for the powerful combination of imaging and genetic fluorescent tools to be applied to the micro-circuitry of mice behaving in flexible virtual environments.

Interpretation of results in context of CAN models

Recent evidence has provided strong support for CAN models as the mechanism underlying the grid cell firing pattern (Couey et al., 2013; Domnisoru et al., 2013; Moser et al., 2014; Pastoll et al., 2013; Stensola et al., 2012; Yoon et al., 2013). In CAN models, grid cells are arranged on a two-dimensional lattice where they uniformly receive feed-forward excitation, which drives firing in the network. Localized "activity bumps" form across the network due to specific patterns of connectivity defined in network space (connection sign and strength versus distance between neurons in the network). While the specific connectivity patterns vary between the different CAN models, network activity bump(s) are always generated, either multiple activity bumps in a triangular grid pattern or single activity bumps (with appropriate boundary conditions). During navigation, the activity bumps are appropriately driven across the network by mouse heading direction and velocity input to lead to grid field firing in the environment.

Assuming that grid cell firing is indeed driven by continuous attractor networks, a comparison between the functional organization of grid cells in network space (the functional organization that arises from their connectivity patterns) and real brain space might provide interesting suggestions about how network space connectivity might map onto real brain space. For example, a similar functional organization in network and brain space would suggest that the pattern of connectivity defined in network space is non-randomly mapped onto real brain space, while dissimilar patterns would suggest more random mapping (though, clearly, functional organization measurements in real brain space do not provide a direct measure of grid cell connectivity). Recent evidence from brain slices demonstrates that layer 2 MEC neurons likely do not share feedback excitation (Couey et al., 2013; Dhillon and Jones, 2000; Pastoll et al., 2013) and are likely connected only through inhibitory interneurons (Beed et al., 2013; Couey et al., 2013; Pastoll et al., 2013). We therefore focused our analysis and interpretation on CAN models that use feedback inhibition (in the form of structured ring(s)) between neighboring grid cells in network space. We implemented a CAN model ((Burak and Fiete, 2009), see Supplemental Methods) in which multiple activity bumps are generated in network space (Burak and Fiete, 2009; Couey et al., 2013; Fuhs and Touretzky, 2006). When the activity bumps were driven across the network in a single direction to model a mouse running along a linear path through its environment (Figure S6A), a Mexican Hat shaped relationship was observed between grid cell-grid cell network connectivity distance and environment firing location correlation (Figure S6A). A qualitatively similar Mexican Hat relationship was also observed for a CAN model generating only a single activity bump (similar to those presented in Guanella et al., 2007; Pastoll et al., 2013) (Figure S6C).

Our experimental data demonstrate a Mexican Hat shaped relationship between grid cell – grid cell distance in MEC and environment firing location correlation that is qualitatively similar to the relationship found in CAN model network space (Figure 4B). Assuming that grid cell networks are indeed connected as proposed by recent CAN models (Burak and Fiete, 2009; Couey et al., 2013; Fuhs and Touretzky, 2006; Guanella et al., 2007; Pastoll et al., 2013), this similarity suggests that grid cells may be, at least partly, anatomically organized in MEC according to their network connectivity pattern.

Though the qualitative shape (Mexican Hat) is similar between our data and that predicted in network space by CAN models, significant differences in the correlation amplitudes exist. For example, the mean correlation for closely neighboring grid cells in MEC was ~0.2 (Figure 4B, 4C) compared to the ~1.0 value predicted by CAN models for closely neighboring neurons in network space (Figure S6A,C). We found that a similar decrease in correlation amplitude can be generated by using a CAN model with partially randomized mapping from network space to physical brain space (Figure S6B). Thus, in the context of CAN models, while the Mexican Hat profile observed in our data suggests that grid cells may be anatomically organized in the MEC according to their network connectivity pattern, the amplitude of the correlations in the profile suggests that some randomization of their anatomical organization likely exists with respect to their network connectivity pattern. The Mexican Hat correlation structure and correlation values close to 1.0 for closely neighboring grid cells are most likely to be observed between grid cells which are members of the same functional module. It is therefore possible that some of the reduction in correlation amplitude may also be due to our imaging fields containing grid cells from different functional modules. Finally, many other grid cell models have been developed (Burgess et al., 2007; Bush and Burgess, 2014; Grossberg and Pilly, 2012; Hasselmo et al., 2007; Mhatre et al., 2012; Zilli and Hasselmo, 2010) and future comparisons between our data and the predictions of these models may also provide interesting suggestions about how network space connectivity might map onto real brain space.

Experimental Procedures

Mouse surgery, virtual reality, and behavior training

All experiments were approved and conducted in accordance with the Northwestern University Animal Care and Use Committee. 7 male C57-BL6 mice (~P70) were anesthetized using 1–2% isofluorane. For virus injection, a small (~0.5 mm) craniotomy was made over the MEC (centered at 3.1 mm lateral from bregma and 0.2 mm rostral from the rostral edge of the transverse sinus). Using a beveled pipette (1–2 MΩ), ~30nL of AAV1-Syn-GCaMP-6f was injected at three depths along the dorsal-ventral axis (1.0, 1.5 and 2.0 mm from the dorsal surface of the brain). 1–2 weeks after the viral injection, a surgery to chronically implant a microprism was performed. Mice were anesthetized and an approximately rectangular craniotomy was made over the dorsal surface of the cortex (above MEC) and cerebellum with corners positioned as follows: 1. ~2.1 mm lateral of bregma, ~4.5 mm caudal of bregma (~300–500 μm rostral of the transverse sinus), 2. ~4.5 mm lateral of bregma, ~4.5 mm caudal of bregma (~300–500 μm rostral of the transvers sinus), 3. ~2.1 mm lateral of bregma, ~7.75–8mm caudal of bregma (~3.25–3.5 mm caudal of the transverse sinus) and 4. ~4.5 mm lateral of bregma, ~7.75–8mm caudal of bregma (~3.25–3.5 mm caudal of the transverse sinus). A portion of the cerebellum (~15–20% of the total cerebellum volume, including portions of the simple lobule, crus 1 and 2 of the ansiform lobule and the paramedian lobule) was removed using suction to expose the caudal surface of the MEC. A thin layer of surgifoam was applied to cover the remaining surface of cerebellum. The tentorium separating the cerebellum and the cortex was then carefully removed using fine forceps, making sure to leave the dura over the MEC completely intact. Tentorium removal was critical for maintaining a clear MEC microprism window over many

weeks to months. A microprism (right angle prism with 1.5 mm side length and reflective enhanced aluminum coating on the hypotenuse, Tower Optical) was mounted on a custom stainless-steel mount (using UV curable adhesive, Norland) (Figure 1A, middle right) and this assembly was then positioned by aligning the front face of the microprism parallel to the caudal surface of the MEC and aligning the top surface of the microprism perpendicular to the (eventual) axis of excitation light propagation. A thin layer of Kwik-Sil was applied to the caudal MEC surface prior to microprism implantation to fill the void between the brain and the front surface of the microprism. The microprism and mount were rigidly held in place and the craniotomy sealed by application of a thin layer of Metabond to all exposed sides of the microprism (except the top surface of the prism) and mount and on any exposed skull or brain. After the metabond cured, the transverse sinus was gently pulled rostral with a custom small aluminum clip (~1.5 mm × ~4.5 mm), which was held in place with superglue (Loctite 401), to ensure a large portion of the top face of the microprism was exposed. Subsequently, a titanium headplate (9.5 mm × 38 mm) was attached to the dorsal surface of the skull, centered upon and aligned parallel to the top face of the microprism. The headplate was used to head restrain the mouse as described previously (Dombeck et al., 2009, 2010). A titanium ring (27 mm outer diameter and 12.5 mm inner diameter, with a 3 mm high edge) was then attached to the top surface of the headplate, centered around the microprism, and the area between the craniotomy and the inner edge of the metal ring was covered with opaque dental cement (Metabond, Parkell, made opaque by adding 0.5 grams of carbon powder, Sigma Aldrich). The metal ring and opaque metabond, combined with the loose fitting black rubber tube and tight fitting metal rings described previously (Dombeck et al., 2010), were required to block stray light from the virtual reality screen.

After the surgery, the mice were allowed to recover in their home cages for ~2–3 days. After this time, the mice began water scheduling (receiving ~1mL of water/day) as described previously (Dombeck et al., 2010; Harvey et al., 2009) and were regularly exposed to a large "playground" with running wheels and tunnels to encourage exploration and locomotion. Some mice displayed motor and locomotion deficits due to the cerebellar lesion, but all mice usually recovered full mobility with limited motor deficits; the "playground" time was found to speed recovery in these mice, but all mice were exposed to the "playground".

Our virtual reality and treadmill system were similar to those previously described (Dombeck et al., 2010; Domnisoru et al., 2013; Harvey et al., 2009), but with the following differences. 5 flat panel IPS LCD monitors (LG IPS235V) were removed from their plastic housing (to minimize bezel width between screens), mounted vertically, and arranged in an approximately half-octagon shape to act as one large continuous screen (using an AMD Radeon HD 6900 video card and AMD Eyefinity software) to display the virtual reality environment (Figure 1B,C). The screens were adjusted for low light emission and were positioned such that the center of each of the 5 screens was ~15 inches from the mouse. The virtual reality environment displayed across the screens covered ~217° and ~67° of the mouse's horizontal and vertical field of view, respectively. The Quake2 video game engine described previously (Domnisoru et al., 2013; Harvey et al., 2009) was used here for the virtual simulation, with minor modifications: the virtual environment was rendered with 5827 × 1920 pixels, and the rendering engine was modified such that the image displayed across the 5 screens had the geometrically correct perspective for the mouse on the

treadmill. Mice were head-restrained with their limbs resting on a freely rotating treadmill consisting of a ~8 inch diameter by 5 inch wide Styrofoam disc with a metal shaft fixed through the disc center (Figure 1B). Low friction ball bearings (SFR155ZZ A7, Dynaroll Corp) were affixed to the ends of the metal shaft and held in place on the optical table using a custom mount.

Mouse locomotion speed on the treadmill was read using a rotary encoder (E2-5000, US Digital used for most experiments; a few early experiments used a E6B2-CWZ3E, Yumo) attached to the metal shaft and used to update forward position in the virtual track, as described previously (Dombeck et al., 2010; Harvey et al., 2009). The movement gain was set such that the full length of the virtual track was traversed by ~6.4 or 8 rotations of the treadmill (4 or 5 m of linear distance, for two different track lengths used here; most experiments used the 5 m track, but a few early experiments used a 4 m track; the single experiment shown in Figure S2 used 3 m and 6 m tracks) and the view angle in the virtual environment was fixed such that the mouse's view was always straight down the center of the track. The rotational velocity of the treadmill (directly related to the mouse's running speed on the treadmill) was linearly related to movement speed along the virtual track. Backward movement on the treadmill was also measured and used to update position (in the backward direction) in the virtual track, however mice almost never moved in the backward direction on the treadmill. Once the mice traversed the full length of the track, they received a small water reward (4 μL) in the track end zone. After the reward and a 2 second delay period, the mouse was "teleported" back to the start of the track to begin another traversal.

Approximately 7 days after surgery, behavior training on the virtual linear track began. Mice were trained ~1hr per day until they routinely ran ~1–3 track traversals/min. The number of days required to reach this criterion varied depending on the mouse and ranged from 2 days to 14 days. Once this criterion was reached, imaging experiments began.

Two-photon Imaging of MEC neurons

A Moveable Objective Microscope (Sutter Instruments) was customized for our imaging experiments. The microscope consisted of a resonant scanning module (Thorlabs), a 20×/ 0.45 NA air immersion objective (correction collar: 1.25) (LUCPlanFL N, Olympus) and enhanced collection optics. Green GCaMP6f fluorescence was routed to a GaAsP PMT (H10770PA-40) using a series of dichroic mirrors and band-pass filters (in order after leaving the back aperture; Semrock): FF665-Di02 long pass dichroic, FF01-680/sp short pass filter, FF560-Di01 long pass dichroic, FF01-510/84 band-pass filter. Stray light from the virtual reality monitor was blocked using a custom box surrounding the top of the microscope objective and the overlying dichroic mirror (not including the tube lens, scan lens, galvos or routing mirrors). This box had one hole on top, for entry of the excitation beam, which was covered with a color glass filter (FGL780, Thorlabs) and one hole on bottom for the microscope objective. This bottom hole was sealed using the same loose black rubber tube and tight fitting metal rings described previously (Dombeck et al., 2010). ScanImage 4 was used for microscope control and acquisition (Pologruto et al., 2003). Ti:Sapphire laser (Chameleon Ultra II, Coherent) light at 920 nm was used as the excitation source. Laser average power at the sample (after the objective) was 120–170 mW. A pockels

cell (350-80-LA-BK-02, 302RM driver, Conoptics) was used to blank laser excitation at the edges of the field of view.

Time-series movies (10,000 frames, 1024×1024 pixels, 0.0678 ms/line or 24,000 frames, 512×512 pixels, 0.0678ms/line) were acquired at 14.4 Hz and 28.8 Hz, respectively. Time-series acquisition was initiated during behavior periods of high-reward rate on the linear track task.

A Digidata1440A (Molecular Devices) data acquisition system was used to record (Clampex 10.3) and synchronize position in the linear track, reward timing, and two-photon image frame timing.

Our microscope was also equipped with a custom wide-field imaging path (IR diode excitation source at 850 nm and CCD camera, Sentech) that was used to locate the prism before two-photon imaging.

Data Analysis

Data was analyzed on a Dell Power Edge 720 Server using ImageJ (Version 1.47) and custom software written in MATLAB (Version R2011a and Version R2013b). All data in the figures are presented as mean ± STD, except in reference to the plots shown in Figures 4C, S2C and S4B where error represents SEM.

To decrease the amount of time required for motion correction, the x and y dimensions of the time-series movies were cropped to a size of ~256-768 × 256-768 pixels. Motion correction on this cropped time-series was performed using whole frame cross-correlation, as described previously (Dombeck et al., 2010; Miri et al., 2011), to generate a set of x and y shifts for each frame of the time-series with respect to a reference frame. These shifts were then applied to the original (non-cropped) time-series to generate the motion corrected time-series used for subsequent analysis.

Regions of interest (ROIs) were defined using Cell Sort (Mukamel et al., 2009). Using the following parameters: threshold = 3–4.5; area limits = 150–4000 pixels; smoothing width = 0.75–1.0; mu = 0.7; Principal Components = 150. All ROIs generated by Cell Sort were visually inspected to select for neuronal somata; any ROIs that appeared to be dendrites were removed from the analysis. F/F versus time traces were generated for each ROI as previously described (Dombeck et al., 2010). Briefly, slow changes in the fluorescence traces were removed by examining the distribution of fluorescence in a ~83.3 sec interval centered around each sample in the trace and normalized by the 8th percentile value. These baseline corrected somatic fluorescence traces were then subjected to the analysis of the ratio of positive to negative going transients of various amplitudes and durations described previously (Dombeck et al., 2007, 2010; Harvey et al., 2009). We used this analysis to identify significant transients with < 1% false positive error rates and generated the significant transient only traces (significant transients left untouched, but all time points between the significant transients are set to 0; seen in Figure 1F top (red), and bottom) that were used for all analysis in this research. Occasionally, multiple ROIs were identified for the same cell (duplicate ROIs) by Cell Sort. If 2 or more ROIs had centroids separated by

less than 15 microns and the Pearson's correlation between the two cells' significant transient only traces was greater than 0.6, then only a one of the ROIs was kept for analysis. The duration of significant transients was computed as the full transient width for each transient and maximum amplitude of significant F/F transients was measured as the largest F/F in each transient.

Here, grid cells were defined based on the classifier developed and outlined in Domnisoru et al (2013). Time points in the significant transient only traces were included in the analysis if they occurred during continuous running periods greater than 30 cm in length in which the running velocity was greater than 1cm/sec. For each cell, the mean F/F was calculated as a function of linear track position in 5 cm bins spanning the length of the track. Candidate In-Grid-Field and Out-of-Grid-Field bins were defined by comparing the mean F/F value in each 5 cm bin to a bootstrap shuffled distribution.

The shuffle distribution was created for each significant transient only trace by randomly shuffling the significant transients and each inter-transient period to generate a new random time series. Inter-transient intervals longer than ¼ of the mean inter-transient interval from the original trace were randomly subdivided until all inter-transient intervals were shorter than ¼ of the original mean. The mean shuffled F/F versus track position in 5 cm bins was generated using the same procedure outlined above. This process was repeated 1000 times to generate a bootstrap shuffled distribution at each 5 cm bin. Both the real and shuffled mean track activity patterns were smoothed using a 3 point Gaussian window with a standard deviation of one. For each bin, a P-value was defined as the number of times the real data mean F/F was greater than the shuffled data mean F/F divided by 1000. Candidate In-Grid-Fields were defined as 3 or more adjacent 5 cm bins each with a P-value 0.85 and with a significant transient occurring in at least one of the bins on at least 20% of all traversals through the field. Candidate Out-of-Grid-Field regions were defined as 2 or more adjacent 5 cm bins each with a P-value 0.25.

Once candidate In-Grid-Field and Out-of-Grid-Field regions were defined, cells were classified as grid cells if they that had 1) at least 3 transitions from In-Grid-Field to Out-of-grid-Field or Out-of-Grid-Field to In-Grid-Field periods, 2) a mean F/F during In-Grid-Field periods that was at least twice that during Out-of-Grid-Field periods, 3) 30% of bins were assigned as either In-Grid-Field or Out-of-Grid-Field, and 4) the widest grid field was less than 100 cm. Grid field widths shown in Figure 2 and Figure S2 were computed as the full In-Grid-Field width as defined above, excluding any fields that did not contain an Out-of-Grid-Field period on each side of the Grid Field. Note that while our track field widths are most likely defined from slices through 2D grid firing fields, the track field widths are not a direct measure of the widths expected in an open field 2D environment. Non-grid cells were defined as any track active cells identified by Cell Sort that were not classified as grid cells (as described above). It should be noted that many cells classified as non-grid cells had spatially selective firing patterns, but did not pass the strict criteria for the grid cell classifier.

The pairwise mean track firing pattern correlations for all classified grid cells and non-grid cells were computed as the Pearson's correlation between the mean F/F versus track position traces (referred to as the mean track firing pattern). The distance between neurons

was measured as the Euclidean distance between the centroids of each neuron's ROI. For data shown in Figure S4, the medial-lateral or dorsal-ventral distances were measured as the distance between the centroids in the x dimension or y dimension, respectively. In order to compare the distribution of pairwise grid cell – grid cell distances to a random distribution, within each field, a random subset of all cells in the field (ie. all grid cells and all non-grid cells) were chosen equal to the number of grid cells identified in that field. All pairwise distances in this randomly selected subset of cells were computed and the mean across all fields was compared to the mean of the real grid cell – grid cell distances. This procedure was repeated 1000 times and the bootstrap P-value was defined as the number of times that the mean of the real grid cell – grid cell distance distribution was above the mean of the bootstrap distribution divided by 1000. To measure the pairwise distance between neurons in either the medial-lateral or dorsal-ventral dimensions to compare the pairwise track firing correlations (shown in Figure S4C and S4D), fields were divided into 4 equally spaced bands (aligned in either the dorsal-ventral or medial-lateral direction). The distance between neuron-neuron pairs was then measured in the medial-lateral or dorsal-ventral dimension only if the centroid of both neurons were contained within a given band. The moving averages shown in Figures 4B and Figure S4A, S4C and S4D (thick-dark lines) were computed by taking the mean of all pairwise correlations contained within a 30 micron pairwise distance window centered upon each micron for distances >20 microns. The binned traces shown in Figures 4B and Figure S4A (thin-dark lines) were computed by binning the pairwise distances into 10 micron bins and taking the mean of all pairwise correlations contained in each bin. The pairwise correlation of the significant F/F time series between non-grid cells revealed a discontinuity (increase in correlation) for pairs of cells < 20 microns apart, which could be caused by fluorescence signal cross-talk. To eliminate any potential for signal crosstalk between closely neighboring neurons, only pairwise track activity pattern correlations from neurons separated by more than 20 microns were included in the analysis. In order to generate the bootstrap shuffled distribution shown in Figure 4B (and Figure S4C,D), within each imaging field the grid cells were left in the same location, but were randomly assigned the mean track firing pattern of a different grid cell. This randomization procedure was repeated 1000 times and the above procedure for calculating correlation versus distance (using the sliding window) was applied to the randomized datasets. A bootstrap P-value was then defined as the number of times the real data mean correlation was greater than (or less than) the randomized distribution mean correlation within the windows (30 μm) around each single micron step divided by 1000.

The relative grid field phase versus pairwise grid cell – grid cell mean 1D slice (traversal) firing correlation shown in Figure S5C was computed by comparing the activity of 9 grid cells with hexagonally arranged Gaussian grid fields (for clarity, only 4 of the 9 cells are displayed in Figure S5A, S5B). The relative phase along a cardinal direction was defined as the distance offset between the spatial activity patterns of grid cell i and grid cell j in the cardinal direction, divided by the distance contained in one period of grid cell i. The correlation was computed as the Pearson's correlation of the mean 1D slice firing patterns between grid cell i and grid cell j, using either on-axis or off-axis traversals.

Supplementary Material

Refer to Web version on PubMed Central for supplementary material.

Acknowledgments

References

Beed P, Gundlfinger A, Schneiderbauer S, Song J, Böhm C, Burgalossi A, Brecht M, Vida I, Schmitz D. Inhibitory gradient along the dorsoventral axis in the medial entorhinal cortex. Neuron. 2013; 79:1197–1207. [PubMed: 24050405]

Bonin V, Histed MH, Yurgenson S, Reid RC. Local Diversity and Fine-Scale Organization of Receptive Fields in Mouse Visual Cortex. J Neurosci. 2011; 31:18506–18521. [PubMed: 22171051]

Brun VH, Solstad T, Kjelstrup KB, Fyhn M, Witter MP, Moser EI, Moser MB. Progressive increase in grid scale from dorsal to ventral medial entorhinal cortex. Hippocampus. 2008; 18:1200–1212. [PubMed: 19021257]

Burak Y, Fiete IR. Accurate path integration in continuous attractor network models of grid cells. PLoS Comput Biol. 2009; 5

Burgalossi A, Herfst L, von Heimendahl M, Förste H, Haskic K, Schmidt M, Brecht M. Microcircuits of Functionally Identified Neurons in the Rat Medial Entorhinal Cortex. Neuron. 2011; 70:773–786. [PubMed: 21609831]

Burgess N, Barry C, O'Keefe J. An oscillatory interference model of grid cell firing. Hippocampus. 2007; 17:801–812. [PubMed: 17598147]

Bush D, Burgess N. A Hybrid Oscillatory Interference/Continuous Attractor Network Model of Grid Cell Firing. J Neurosci. 2014; 34:5065–5079. [PubMed: 24695724]

Chen TW, Wardill TJ, Sun Y, Pulver SR, Renninger SL, Baohan A, Schreiter ER, Kerr Ra, Orger MB, Jayaraman V, et al. Ultrasensitive fluorescent proteins for imaging neuronal activity. Nature. 2013; 499:295–300. [PubMed: 23868258]

Chia TH, Levene MJ. Microprisms for in vivo multilayer cortical imaging. J Neurophysiol. 2009; 102:1310–1314. [PubMed: 19494189]

Couey JJ, Witoelar A, Zhang SJ, Zheng K, Ye J, Dunn B, Czajkowski R, Moser MB, Moser EI, Roudi Y, et al. Recurrent inhibitory circuitry as a mechanism for grid formation. Nat Neurosci. 2013; 16:318–324. [PubMed: 23334580]

Dhillon A, Jones RSG. Laminar differences in recurrent excitatory transmission in the rat entorhinal cortex in vitro. Neuroscience. 2000; 99:413–422. [PubMed: 11029534]

Dombeck DA, Reiser MB. Real neuroscience in virtual worlds. Curr Opin Neurobiol. 2012; 22:3–10. [PubMed: 22138559]

Dombeck DA, Khabbaz AN, Collman F, Adelman TL, Tank DW. Imaging Large-Scale Neural Activity with Cellular Resolution in Awake, Mobile Mice. Neuron. 2007; 56:43–57. [PubMed: 17920014]

Dombeck DA, Graziano MS, Tank DW. Functional clustering of neurons in motor cortex determined by cellular resolution imaging in awake behaving mice. J Neurosci. 2009; 29:13751–13760. [PubMed: 19889987]

Dombeck DA, Harvey CD, Tian L, Looger LL, Tank DW. Functional imaging of hippocampal place cells at cellular resolution during virtual navigation. Nat Neurosci. 2010; 13:1433–1440. [PubMed: 20890294]

Domnisoru C, Kinkhabwala AA, Tank DW. Membrane potential dynamics of grid cells. Nature. 2013; 495:199–204. [PubMed: 23395984]

Fuhs MC, Touretzky DS. A spin glass model of path integration in rat medial entorhinal cortex. J Neurosci. 2006; 26:4266–4276. [PubMed: 16624947]

Fyhn M, Molden S, Witter MP, Moser EI, Moser MB. Spatial representation in the entorhinal cortex. Science. 2004; 305:1258–1264. [PubMed: 15333832]

Fyhn M, Hafting T, Witter MP, Moser EI, Moser MB. Grid cells in mice. Hippocampus. 2008; 18:1230–1238. [PubMed: 18683845]

Garden DLF, Dodson PD, O'Donnell C, White MD, Nolan MF. Tuning of Synaptic Integration in the Medial Entorhinal Cortex to the Organization of Grid Cell Firing Fields. Neuron. 2008; 60:875–889. [PubMed: 19081381]

Giocomo LM, Zilli EA, Fransén E, Hasselmo ME. Temporal frequency of subthreshold oscillations scales with entorhinal grid cell field spacing. Science. 2007; 315:1719–1722. [PubMed: 17379810]

Göbel W, Helmchen F. New angles on neuronal dendrites in vivo. J Neurophysiol. 2007; 98:3770–3779. [PubMed: 17898141]

Grossberg S, Pilly PK. How Entorhinal Grid Cells May Learn Multiple Spatial Scales from a Dorsoventral Gradient of Cell Response Rates in a Self-organizing Map. PLoS Comput Biol. 2012; 8

Guanella A, Kiper D, Verschure P. A model of grid cells based on a twisted torus topology. Int J Neural Syst. 2007; 17:231–240. [PubMed: 17696288]

Hafting T, Fyhn M, Molden S, Moser MB, Moser EI. Microstructure of a spatial map in the entorhinal cortex. Nature. 2005; 436:801–806. [PubMed: 15965463]

Hafting T, Fyhn M, Bonnevie T, Moser MB, Moser EI. Hippocampus-independent phase precession in entorhinal grid cells. Nature. 2008; 453:1248–1252. [PubMed: 18480753]

Harvey CD, Collman F, Dombeck DA, Tank DW. Intracellular dynamics of hippocampal place cells during virtual navigation. Nature. 2009; 461:941–946. [PubMed: 19829374]

Harvey CD, Coen P, Tank DW. Choice-specific sequences in parietal cortex during a virtual-navigation decision task. Nature. 2012; 484:62–68. [PubMed: 22419153]

Hasselmo ME, Giocomo LM, Zilli EA. Grid cell firing may arise from interference of theta frequency membrane potential oscillations in single neurons. Hippocampus. 2007; 17:1252–1271. [PubMed: 17924530]

Henze DA, Borhegyi Z, Csicsvari J, Mamiya A, Harris KD, Buzsáki G. Intracellular features predicted by extracellular recordings in the hippocampus in vivo. J Neurophysiol. 2000; 84:390–400. [PubMed: 10899213]

Hira R, Ohkubo F, Ozawa K, Isomura Y, Kitamura K, Kano M, Kasai H, Matsuzaki M. Spatiotemporal dynamics of functional clusters of neurons in the mouse motor cortex during a voluntary movement. J Neurosci. 2013; 33:1377–1390. [PubMed: 23345214]

Issa JB, Haeffele BD, Agarwal A, Bergles DE, Young ED, Yue DT. Multiscale optical ca(2+) imaging of tonal organization in mouse auditory cortex. Neuron. 2014; 83:944–959. [PubMed: 25088366]

Ji N, Sato TR, Betzig E. Characterization and adaptive optical correction of aberrations during in vivo imaging in the mouse cortex. Proc Natl Acad Sci. 2012; 109:22–27. [PubMed: 22190489]

Katona G, Szalay G, Maák P, Kaszás A, Veress M, Hillier D, Chiovini B, Vizi ES, Roska B, Rózsa B. Fast two-photon in vivo imaging with three-dimensional random-access scanning in large tissue volumes. Nat Methods. 2012; 9:201–208. [PubMed: 22231641]

Kitamura T, Pignatelli M, Suh J, Kohara K, Yoshiki A, Abe K, Tonegawa S. Island cells control temporal association memory. Science. 2014; 343:896–901. [PubMed: 24457215]

Komiyama T, Sato TR, O'Connor DH, Zhang YX, Huber D, Hooks BM, Gabitto M, Svoboda K. Learning-related fine-scale specificity imaged in motor cortex circuits of behaving mice. Nature. 2010; 464:1182–1186. [PubMed: 20376005]

Lewallen SJ, Yoon K, Kinkhabwala AA, Domnisoru C, Tank DW, Feite I. 1D grid fields are slices of a 2D hexagonal lattice. Soc Neurosci Abstr. 2013; 39:94.04.

Mechler F, Victor JD, Ohiorhenuan I, Schmid AM, Hu Q. Three-dimensional localization of neurons in cortical tetrode recordings. J Neurophysiol. 2011; 106:828–848. [PubMed: 21613581]

Mhatre H, Gorchetchnikov A, Grossberg S. Grid cell hexagonal patterns formed by fast self-organized learning within entorhinal cortex. Hippocampus. 2012; 22:320–334. [PubMed: 21136517]

Miri A, Daie K, Burdine RD, Aksay E, Tank DW. Regression-based identification of behavior-encoding neurons during large-scale optical imaging of neural activity at cellular resolution. J Neurophysiol. 2011; 105:964–980. [PubMed: 21084686]

Moser EI, Roudi Y, Witter MP, Kentros C, Bonhoeffer T, Moser MB. Grid cells and cortical representation. Nat Rev Neurosci. 2014; 15:466–481. [PubMed: 24917300]

Mukamel EA, Nimmerjahn A, Schnitzer MJ. Automated Analysis of Cellular Signals from Large-Scale Calcium Imaging Data. Neuron. 2009; 63:747–760. [PubMed: 19778505]

Pastoll H, Solanka L, van Rossum MCW, Nolan MF. Feedback Inhibition Enables Theta-Nested Gamma Oscillations and Grid Firing Fields. Neuron. 2013; 77:141–154. [PubMed: 23312522]

Pologruto TA, Sabatini BL, Svoboda K. ScanImage: flexible software for operating laser scanning microscopes. Biomed Eng Online. 2003; 2:13. [PubMed: 12801419]

Ray S, Naumann R, Burgalossi A, Tang Q, Schmidt H, Brecht M. Grid-layout and theta-modulation of layer 2 pyramidal neurons in medial entorhinal cortex. Science. 2014; 343:891–896. [PubMed: 24457213]

Redish AD, Battaglia FP, Chawla MK, Ekstrom AD, Gerrard JL, Lipa P, Rosenzweig ES, Worley PF, Guzowski JF, McNaughton BL, et al. Independence of firing correlates of anatomically proximate hippocampal pyramidal cells. J Neurosci. 2001; 21:RC134. [PubMed: 11222672]

Sato TR, Gray NW, Mainen ZF, Svoboda K. The functional microarchitecture of the mouse barrel cortex. PLoS Biol. 2007; 5:1440–1452.

Sawinski J, Wallace DJ, Greenberg DS, Grossmann S, Denk W, Kerr JND. Visually evoked activity in cortical cells imaged in freely moving animals. Proc Natl Acad Sci U S A. 2009; 106:19557–19562. [PubMed: 19889973]

Schmidt-Hieber C, Häusser M. Cellular mechanisms of spatial navigation in the medial entorhinal cortex. Nat Neurosci. 2013; 16:325–331. [PubMed: 23396102]

Stensola H, Stensola T, Solstad T, Frøland K, Moser MB, Moser EI. The entorhinal grid map is discretized. Nature. 2012; 492:72–78. [PubMed: 23222610]

Varga C, Lee SY, Soltesz I. Target-selective GABAergic control of entorhinal cortex output. Nat Neurosci. 2010; 13:822–824. [PubMed: 20512133]

Yoon K, Buice Ma, Barry C, Hayman R, Burgess N, Fiete IR. Specific evidence of low-dimensional continuous attractor dynamics in grid cells. Nat Neurosci. 2013; 16:1077–1084. [PubMed: 23852111]

Yoon K, Lewallen S, Kinkhabwala AA, Tank DW, Fiete I. Grid cell response in 1D environments are consisten with 2D continuous attractor dynamics. Soc Neurosci Abstr. 2013; 39:94.05.

Zilli EA, Hasselmo ME. Coupled noisy spiking neurons as velocity-controlled oscillators in a model of grid cell spatial firing. J Neurosci. 2010; 30:13850–13860. [PubMed: 20943925]

Ziv Y, Burns LD, Cocker ED, Hamel EO, Ghosh KK, Kitch LJ, El Gamal A, Schnitzer MJ. Long-term dynamics of CA1 hippocampal place codes. Nat Neurosci. 2013; 16:264–266. [PubMed: 23396101]
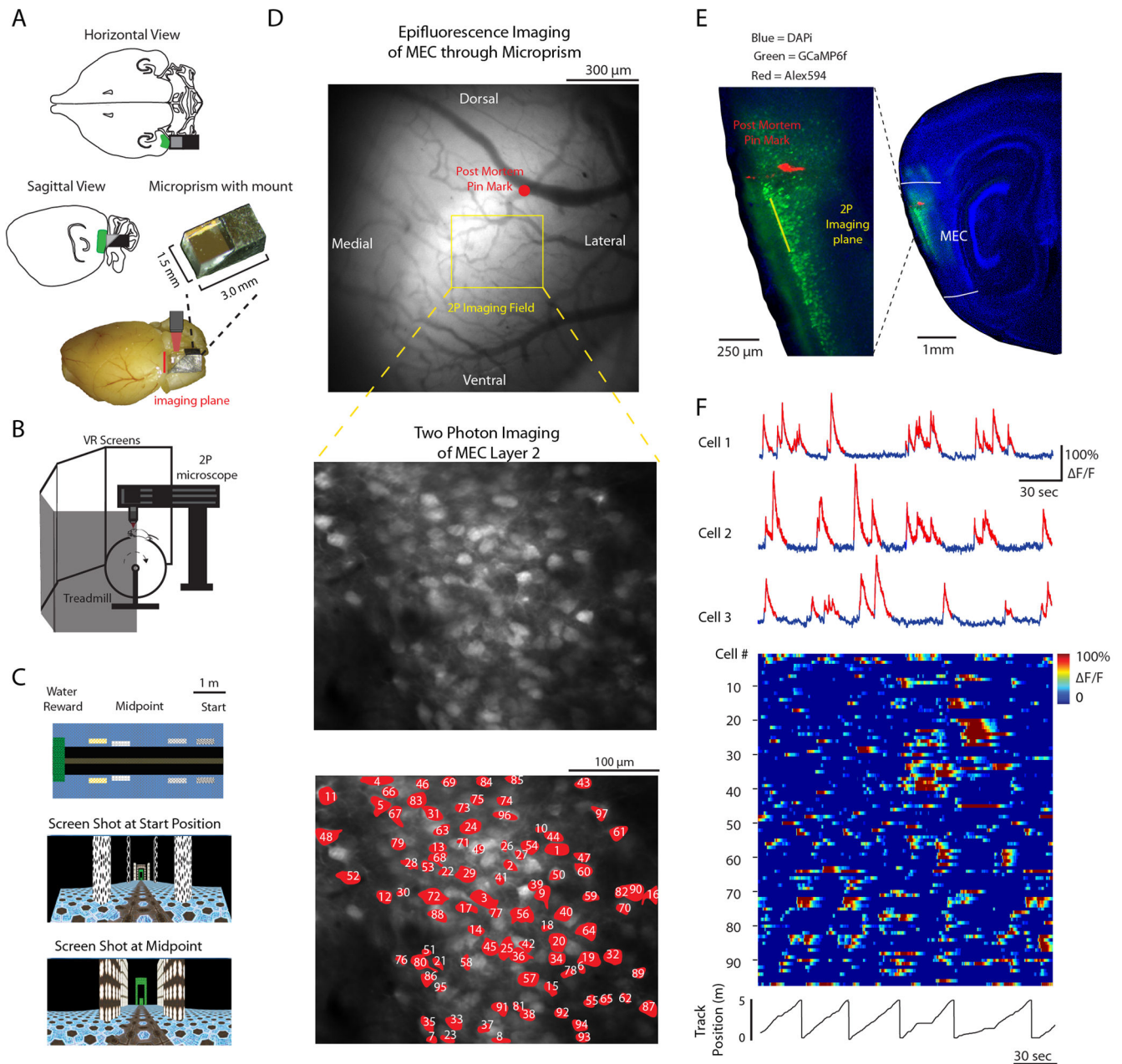
Figure 1.
Cellular-resolution imaging of neuronal activity in MEC during navigation along a virtual linear track. **A.** Horizontal (top) and sagittal (middle, left) schematics depicting microprism placement for imaging medial entorhinal cortex (MEC, green); a microprism-mount assembly is shown alone (middle, right) and positioned on a fixed mouse brain to show the approximate positioning used during imaging experiments (bottom). **B.** Schematic showing two-photon microscope and virtual reality system. **C.** 5 m virtual linear track layout (top view, top; screenshots, middle and bottom); mouse runs from start position to the reward location (green) where it is "teleported" back to start location. **D.** Top, epifluorescence image of GCaMP-6f fluorescence through chronic MEC microprism in awake mouse.

Location of two-photon imaging field (yellow box) and of post-mortem Alexa-594 pin-mark labeling (red dot) are shown. Middle and bottom, Field of layer 2 MEC neurons (from region shown in **D** top) labeled with GCaMP-6f and imaged through MEC microprism with two-photon microscopy. **E.** Sagittal section (post-mortem) used to verify imaging plane location (yellow) as MEC (identified from pin marking, red, in **D**) shows GCaMP-6f labeled neurons in MEC (green) and morphology from DAPi staining (blue). **F.** GCaMP-6f F/F traces from 3 neurons (blue, top; significant transients highlighted in red) and activity patterns from 97 active neurons (bottom, significant transients only) labeled in **D** (bottom). Time-series data acquired during virtual track traversals (bottom).
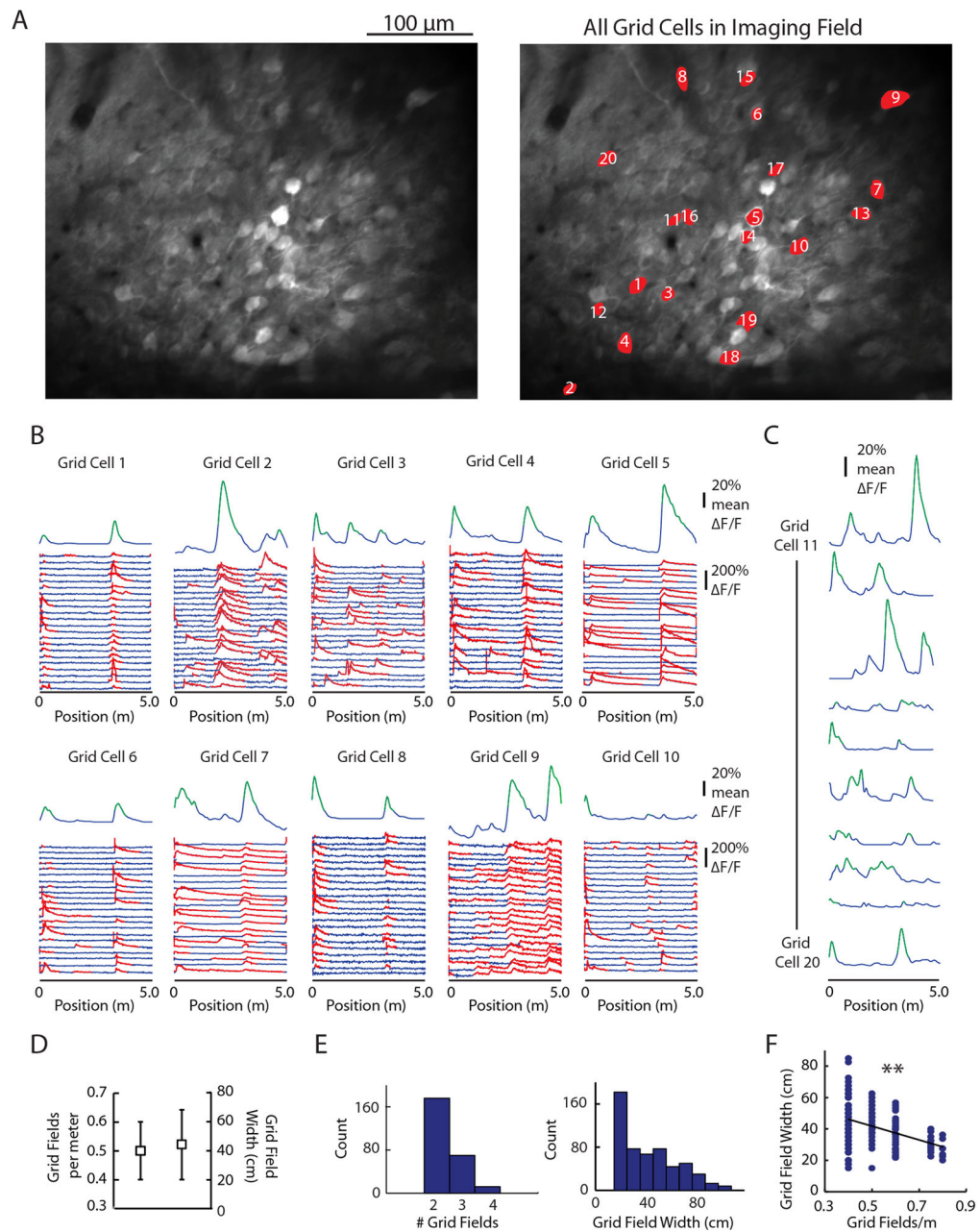
Figure 2.
Cellular-resolution imaging of MEC grid cells. **A.** Field of layer 2 MEC neurons labeled with GCaMP-6f and imaged through MEC microprism with two-photon microscopy. **B.** GCaMP-6f F/F versus linear track position traces for 10 grid cells shown in Figure 2A. Each of the 22 track traversals is shown for each of the 10 cells (bottom, significant transients highlighted in red) along with the mean of F/F versus track position for all traversals (top), this mean trace is referred to as the mean track firing pattern. Significant grid fields highlighted in green. **C.** Mean of F/F versus track position for all other grid cells shown in Figure 2A. **D.** Grid fields per meter and field width for all 259 grid cells (mean ± STD). **E.** Histograms of number of grid fields (left) and field widths (right) for all grid cells.

F. Field width decreases with increasing fields per meter (n = 259 grid cells, P < 0.01 Spearman Rank Correlation Coefficient).
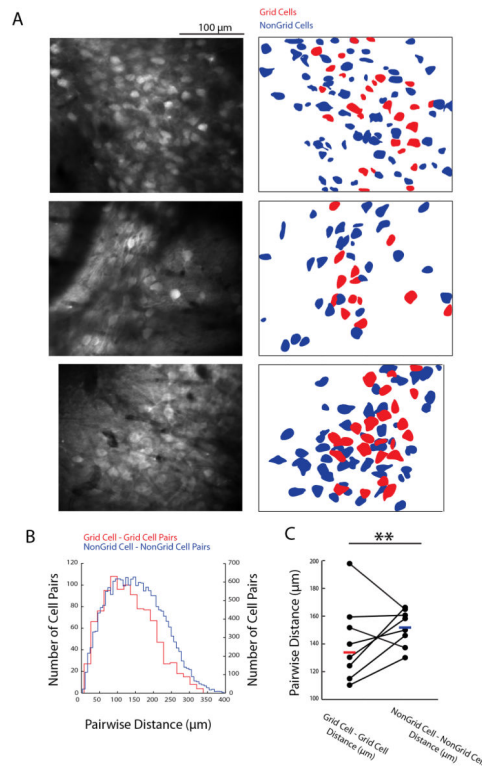
Figure 3.
Grid cells are physically clustered in MEC with respect to non-grid cells. **A.** 3 example fields (left) and all identified grid cells (red) and non-grid cells (blue) for each field (right). **B.** Histogram of distances measured between grid cell - grid cell pairs (red) and non-grid cell – non-grid cell pairs (blue) across 8 imaging fields with similar size. **C.** Mean grid cell – grid cell distance and non-grid cell – non-grid cell distance for each of the 8 fields and the mean (colored lines) for all fields (P < 0.01, Student's T-Test).
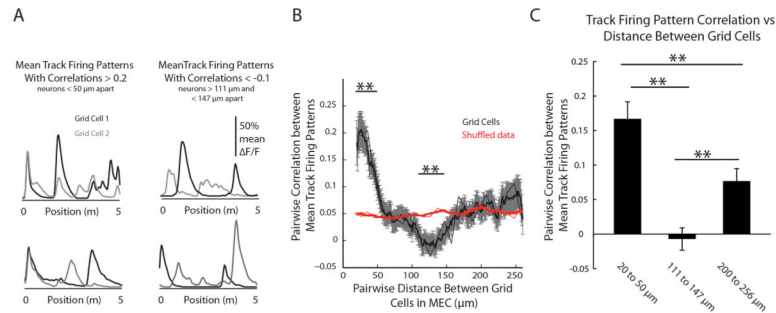
Figure 4.
A Mexican Hat shaped relationship exists between grid cell-grid cell distance and mean track firing pattern correlation. **A.** Examples of higher (left) and lower (right) correlations between mean track firing patterns (mean of ΔF/F versus track position) of nearby (left) and mid-distance (right) grid cell pairs. **B.** Plot of mean grid cell – grid cell distance versus mean track firing pattern correlation averaged over all grid cells in all acquired time-series (black). Same plot is also shown for a randomized data set in which grid cells were left in the same location but were randomly assigned the mean track firing pattern of a different grid cell (red). Thick dark line represents moving average (30 micron window) with light bands depicting SEM. Thin dark line represents mean of data binned at 10 micron increments. ** denotes P < 0.01, from bootstrapping. **C.** Mean track firing pattern correlation for grid cells separated by 20–50 μm, 111–147 μm, and 200–256 μm. ** denotes P < 0.01, Tukey-Kramer. Error bars indicate SEM.